

1 **Insights into the vulnerability of vegetation to tephra** 2 **fallouts from interpretable machine learning and big** 3 **Earth observation data**

4 Sébastien Biass^{1,2}, Susanna F. Jenkins^{1,3}, William H. Aeberhard⁴, Pierre Delmelle⁵, Thomas
5 Wilson⁶

6 ¹ *Earth Observatory of Singapore, Nanyang Technological University, Singapore*

7 ² *Department of Earth Sciences, University of Geneva, Switzerland*

8 ³ *Asian School of the Environment, Nanyang Technological University, Singapore*

9 ⁴ *Swiss Data Science Center, ETH Zürich, Switzerland*

10 ⁵ *Environmental Sciences, Earth and Life Institute, UCLouvain, Belgium*

11 ⁶ *School of Earth and the Environment, University of Canterbury, New Zealand*

12 Corresponding author: Sébastien Biass (sebastien.biass@unige.ch)

13 **Keywords** : Big EO data ; interpretable machine learning ; volcanic hazards; vulnerability
14 model; vegetation impact; natural hazards; disaster risk reduction; Google Earth Engine;

15 **Abstract**

16 Although the generally high fertility of volcanic soils is often seen as an opportunity, short-
17 term consequences of eruptions on natural and cultivated vegetation are likely to be negative.

18 The empirical knowledge obtained from post-event impact assessments provides crucial
19 insights into the range of parameters controlling impact and recovery of vegetation, but their
20 limited coverage in time and space offers a limited sample of all possible eruptive and
21 environmental conditions. Consequently, vegetation vulnerability remains largely
22 unconstrained, thus impeding quantitative risk analyses.

23 Here, we explore how cloud-based big Earth Observation data, remote sensing and interpretable
24 machine learning (ML) can provide a large-scale alternative to identify the nature of, and infer
25 relationships between, drivers controlling vegetation impact and recovery. We present a
26 methodology developed using Google Earth Engine to systematically revisit the impact of past

27 eruptions and constrain critical hazard and vulnerability parameters. Its application to the
28 impact associated with the tephra fallout from the 2011 eruption of Cordón Caulle volcano
29 (Chile) reveals its ability to capture different impact states as a function of hazard and
30 environmental parameters and highlights feedbacks and thresholds controlling impact and
31 recovery of both natural and cultivated vegetation. We therefore conclude that big EO data and
32 machine learning complement existing impact datasets and open the way to a new type of
33 dynamic and large-scale vulnerability models.

34 **1. Introduction**

35 In 2015, more than 8% of the world's population lived within 100 km of a volcano that had a
36 significant eruption during the Holocene (Freire et al., 2019). Current trends indicate that this
37 exposure will increase with, for instance, the population in the two regions most exposed to
38 volcanic hazards (i.e. SE Asia and Central America) having doubled since 1975 (Freire et al.,
39 2019). Supporting up to 10% of the world's population, the fertility of volcanic soils partly
40 contributes to these increasing demographics (Rampengan et al., 2016, Loughlin et al., 2018).
41 However, farming systems remain subject to short-term negative impacts from volcanic hazards
42 (Choumert and Phinélias, 2018; Few et al., 2017; Phillips et al., 2019; Sivarajan et al., 2017).
43 Recent, modest-sized eruptions over the past decade have illustrated the large numbers of
44 people affected by volcanic activity, and the losses associated with impacts to agriculture, in
45 particular the crop subsector. For example, the 2020 VEI 4 (Volcanic Explosivity Index,
46 Newhall and Self, 1982) eruption of Taal (Philippines) affected ~260,000 people and caused an
47 estimated 63 million USD impact on agriculture (ReliefWeb, 2020), whereas the 2018 eruption
48 of Fuego (Guatemala), also a VEI 4, indirectly affected ~1.7 million people and caused ~58
49 million USD impact on agriculture (The World Bank, 2018). By comparison, a recent study by
50 Jenkins et al (2022) estimates that on the island of Java in Indonesia only, a VEI 4 eruption has

51 a 50% probability of directly affecting ≥ 5 million people and ~ 700 km² of crops, which
52 increases to ~ 29 million people and 12,000 km² of crops for an eruption of VEI 5.

53 The Food and Agriculture Organisation (FAO, 2018) notes how the absence of a systematic
54 and in-depth documentation of the impacts of natural hazards on agriculture prevents acquiring
55 a global understanding of their long-term direct and indirect as well as tangible and intangible
56 consequences. This is especially true for volcanic risk. Our current knowledge of the
57 vulnerability of agriculture to volcanic hazards comes from a combination of opportunistic
58 field-based post-event impact assessments (post-EIA; e.g., Blake et al., 2015; Le Penneec et al.,
59 2012; Magill et al., 2013; Phillips et al., 2019; Stewart et al., 2016; Wilson et al., 2011; Wilson
60 et al., 2013) and rarer experimental studies (Hotes et al., 2004; Zobel et al., 2022; Ligot et al.,

Deleted: even

Formatted: French (Switzerland)

61 in prep.). However, the generalisation of these empirical lessons is limited by two main aspects.
62 Firstly, eruptions are relatively infrequent but display a wide range of behaviours, each of which
63 has specific hazard, hazard characteristics, and impact mechanisms. Secondly, they occur over
64 a large variety of climates and affect various vegetation types and agricultural practices.
65 Damage/disruption states (DDS) derived from these data (e.g., Craig et al., 2021; Jenkins et al.,
66 2015; Table 1) have contributed to identifying critical components of vulnerability, but
67 currently remain too limited in time and space to allow for the development of accurate and
68 generalised risk models.

Deleted: Table 1

69 Satellite-based Earth Observation (EO) data, on the other hand, provide a data acquisition
70 framework that is both global in space and consistent in time. Missions such as Landsat,
71 MODIS or Sentinel now provide decades of global EO data at constantly increasing spatial,
72 temporal and spectral resolutions. Monitoring of the spectral characteristics of vegetation using
73 these missions has been used to assess the recovery of vegetation after earthquakes (Chou et
74 al., 2009; Lu et al., 2012) and droughts (Rembold et al., 2019) or to derive global-scale datasets

Deleted: five

Deleted: a

79 to estimate food security (Meroni et al., 2019). In volcanic contexts, satellite imagery has been
80 used to capture the impact of eruptions on vegetation (de Rose et al., 2011; De Schutter et al.,
81 2015; Easdale and Bruzzone, 2018; Li et al., 2018; Marzen et al., 2011; Tortini et al., 2017).
82 Although innovative, these attempts mostly relied on single case studies, simplified
83 representations of hazards and never systematically investigated the range of factors controlling
84 the impact and recovery. The dominant limitation behind this latter point is a data processing
85 issue: despite the availability of an unprecedented variety of data through EO, this big EO data
86 is associated with new challenges regarding data access, storage and processing. These
87 challenges have prevented the systematic investigation of the nature and the relationship
88 between the various processes controlling vulnerability and impact of vegetation to volcanic
89 hazard from a global remote sensing perspective.

90 However, the recent advent of cloud-based EO data storage and processing platforms paves the
91 way for the development of methodologies that can exploit the full potential of big EO data
92 (Giuliani et al., 2019; Gomes et al., 2020; Mahecha et al., 2020). Beyond providing a framework
93 for data-intensive research, big EO data platforms contribute to systematically extracting and
94 processing raw data into information and knowledge (Lehmann et al., 2020; Nativi et al., 2020;
95 Rowley, 2007). Over the past five years, *Google Earth Engine* (GEE; Gorelick et al., 2017) has
96 seen the highest increase in applications reported in the scientific literature. GEE provides
97 access and a computing power to process big EO data enabling reproducible, global scale
98 analyses (Tamiminia et al., 2020; Wang et al., 2020). GEE has been applied to aspects of natural
99 vegetation dynamics (Campos-Taberner et al., 2018; Kong et al., 2019; Zhang et al., 2019),
100 crop mapping and monitoring (Jin et al., 2019; Liu et al., 2020), land cover-land use
101 classification (Khanal et al., 2020), food security (Poortinga et al., 2018; Rembold et al., 2019)
102 and hazard mapping (Crowley et al., 2019; DeVries et al., 2020). In a volcanic context, the use
103 of GEE remains limited to a few applications (e.g., Biass et al., 2021; Murphy et al., 2017).

Formatted: French (Switzerland)

Field Code Changed

Deleted:

Deleted: large

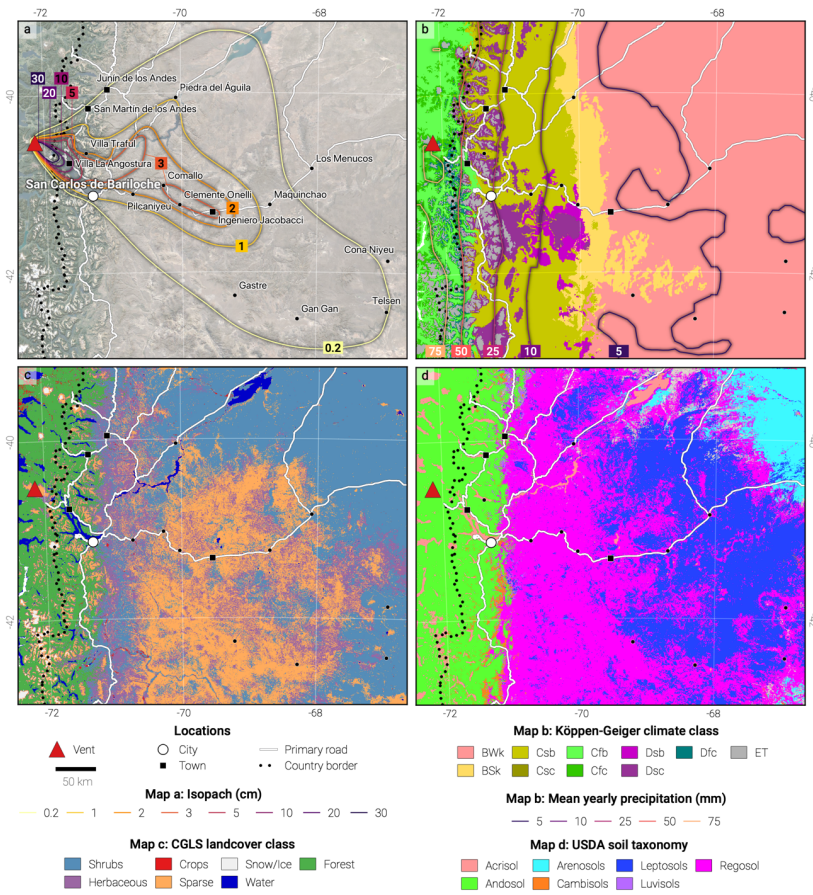
Deleted: set

107 We argue that the advent of open-access cloud-based EO data platforms combined with
108 increasingly efficient empirical modelling approaches offer an unprecedented opportunity to
109 investigate the fragility of vegetation, including agricultural crops, to diverse events like
110 volcanic eruptions, where field studies spanning the large spatial and temporal impact spaces
111 are typically not possible. Here we lay the foundation of a methodology to extract previously
112 unexploited knowledge about the impact to, and recovery of, vegetation from past eruptions
113 recorded in archives of multi-spectral images. In line with the challenges identified by the FAO
114 (FAO, 2018), this methodology is designed to support a framework to i) unify indirect, global
115 with direct, *in situ* observations of impacts and ii) develop an innovative type of evidence-
116 based, EO-driven vulnerability model. Both factors will improve our empirical knowledge
117 around vegetation impacts and recovery following volcanic eruptions, supporting evidence-
118 based assessments for future eruptions.

119 Here we focus on the impacts to vegetation caused by the widespread tephra fallout deposits
120 from the 2011 eruption of Cordon Caulle volcano (Chile). The main steps include i)
121 reconstructing the relevant hazard impact metrics of the associated tephra fallout deposit using
122 dedicated numerical models, ii) mapping vegetation impact using time series of MODIS images
123 retrieved from GEE, iii) identifying and processing selected datasets and variables on GEE to
124 build up a big EO dataset of proxies capturing the dynamics of vulnerability in space and time,
125 iv) developing a flexible machine learning (ML) algorithm trained to explain impact as a
126 function of the covariates and v) interpreting the model's result to investigate the nature,
127 importance and relationships between the different hazard and vulnerability proxies using
128 dedicated libraries.

129 **Table 1** : Damage/disruption states (DS1–5) as a function of the dry deposit thickness as hazard proxy identified
130 by Jenkins et al., (2014) based on literature review. DDS assume that crops are in the growing stage. Hazard
131 metrics include the median and interdecile deposit thicknesses inferred from expert judgement and empirical data.

Deleted: to



134

135 Figure 1: Overview map of the study area. a Isopach (cm) from Dominguez and Baumann (personal
 136 communication) showing lines of equal thickness of the fallout deposit for the month of June 2011. Locations are
 137 those mentioned in Elissondo et al., (2016) as being affected by tephra fall. Background is © Google Maps 2022.
 138 Roads, locations and borders are from © OpenStreetMap contributors 2021. Distributed under the Open Data
 139 Commons Open Database License (ODbL) v1.0. b Mean yearly precipitation (mm) for the period 2006-2011
 140 inferred from ERA5. Note that these values differ from those presented in the text and in Elissondo et al., (2016)
 141 as ERA5 values represent averages over a model grid cell and time step. Background is the Köppen-Geiger climate
 142 classification of Beck et al., (2018). *BWk* - Arid, desert, cold arid, *BSk* - Arid, steppe, cold arid, *Cfb* - Warm
 143 temperate, fully humid, warm summer, *Cfc* - Warm temperate, fully humid, cool summer, *Csb* - Warm temperate,
 144 summer dry, warm summer, *Csc* - Warm temperate, summer dry, cool summer, *Dsb* - Snow, summer dry, warm

Deleted: cumulative

Deleted: s

147 summer, *Dsc* - Snow, summer dry, cool summer, *ET* - Polar, polar tundra. **c** Landcover classes from the CGLS–
148 LC1000 dataset (Buchhorn et al., 2020). **d** Dominant soil types in the study area from the SoilGrid dataset (Hengl
149 et al., 2017) based on the USDA soil taxonomy. All maps are projected using EPSG:32719.

150 **2. Background**

151 **2.1. Impact of volcanic hazards on vegetation**

152 Explosive volcanic eruptions produce *tephra*, a generic term for pyroclasts originating from the
153 fragmentation of parent magma, the fraction <2 mm diameter of which is referred to as *ash*. For
154 sufficiently large eruptions, tephra deposits can alter the hydrology, vegetation cover and soil
155 properties of entire regions, contributing to the perturbation of their ecosystems for months-
156 years (Major et al., 2016; Pierson et al., 2013; Zobel et al., 2022). Direct negative impacts on,
157 and the ability of vegetation to recover from eruptions depends on complex interactions
158 between biotic and abiotic parameters (Ayrís and Delmelle, 2012; Arnalds, 2013). Biotic
159 parameters include the type and composition of the vegetation, the biological legacy related to
160 previous stresses and the phenological state of the plant at the time of eruption (Jenkins et al.,
161 2014a; Ligot et al., 2022). Abiotic parameters include climate (e.g. rainfall and temperature)
162 and environmental setting (e.g. elevation, slope, orientation) (Crisafulli et al., 2015; Dale et al.,
163 2005). For crops, impacts also depend on access to technology and mitigation measures (Magill
164 et al., 2013; Wilson et al., 2013a). Mechanisms of adverse effects of tephra on vegetation are
165 various, including smothering and burial, breaking and abrasion, reduced photosynthesis, salt-
166 induced stress and limitation of pollination (Arnalds, 2013; Ayrís and Delmelle, 2012; Blake et
167 al., 2015). **Critical hazard impact metrics therefore** depend on the characteristics of the eruption
168 (e.g., magnitude, intensity and style) and the **properties of the** deposit (i.e., thickness, grainsize
169 distribution, content in water-soluble elements) (Cronin et al., 2014; Stewart et al., 2016). ▼

Deleted: Finally, impacts also

Deleted: Overall, tephra on crops perturbate plant phenology and may decrease or even annihilate crop production (Ligot et al., 2022; Wilson et al., 2007).

174 **2.2. Case study: The Puyehue–Cordón Caulle 2011 eruption**

175 On June 4 2011, a subplinian rhyolitic eruption started at Cordón Caulle volcano (CC; 40.525
176 S, 72.16 W; [Figure 1](#)), part of the Puyehue–Cordón Caulle volcanic complex. The eruption
177 began with a 24-30 h-long paroxysmal phase that gradually transitioned to low intensity tephra
178 emissions lasting for several months (Pistolesi et al., 2015). Reported plume heights ranged
179 from 9–12 km asl for the first 3–4 days, 4–9 km asl for the following week and <4 km asl after
180 June 14 (Bonadonna et al., 2015; Collini et al., 2013). During the first week, westerly winds
181 dispersed ~1 km³ of tephra towards Argentina. Published isopach maps describe the deposit
182 thickness associated with various phases of the eruption (e.g. Bonadonna et al., 2015; Collini
183 et al., 2013). An unpublished report by Dominguez and Baumann (personal communication),
184 combining data from Bonadonna et al., (2015) and Pistolesi et al., (2015), shows the spatial
185 distribution of total deposit thickness for June 4–30 2011 ([Figure 1a](#)). [The deposit showed low](#)
186 [to very low concentrations of water-soluble elements potentially harmful to plant leaves \(e.g.,](#)
187 [fluorine sulphur;](#) Stewart et al., 2016).

188 The deposit of the CC 2011 eruption impacted three different [biogeographical regions](#): from
189 west to east, southern Andes, Andean foothills and lowlands (Elissondo et al., 2016). These
190 roughly correspond to the *Warm temperate – fully humid*, *Warm temperate – summer dry* and
191 *Arid* climate classifications ([Figure 1](#); Beck et al., 2018), respectively, each characterized by
192 specific assemblages of vegetation (Easdale and Bruzzone, 2018; Enriquez et al., 2021).
193 Southern Andes are characterized by a high elevation (mean of 2000 m asl), Valdivian
194 temperate forest and annual precipitation, of 800–2500 mm, mainly occurring in June–August
195 (Elissondo et al., 2016). Andean foothills are characterized by a gradient of annual precipitation
196 decreasing from 800 in the west to 300 mm in the east and a vegetation of grasses, shrubs, and
197 wet meadows covering 5–10 % of the area (Easdale and Bruzzone, 2018; Elissondo et al.,
198 2016). The lowland is characterized by a cold and semi-arid climate with annual precipitation,

Deleted: Figure 1

Deleted: Figure 1

Deleted: Levels of all

Deleted: extractable

Deleted: of the 2011 Cordón Caulle tephra were low to very-low...

Deleted: (

Deleted: ecosystems

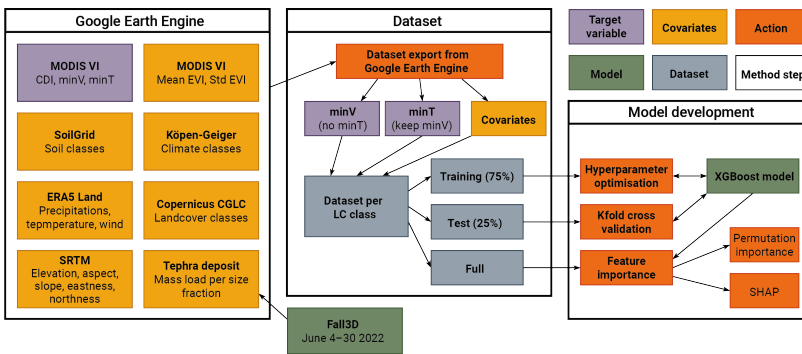
Deleted: Figure 1

Deleted: s

Deleted: s

210 of ≤ 300 mm. During the six years prior to the eruption, this region experienced < 160 mm of
 211 precipitation per year, which caused regional drought conditions. Due to water availability, the
 212 rainfall gradient strongly controls the type of farming, with pastoral farming and agriculture in
 213 Andean regions and low intensity goat and sheep farming in the arid lowlands (Stewart et al.,
 214 2016). In addition, regions with low precipitation experience wind erosion and remobilization
 215 of loose tephra (Dominguez et al., 2020b; Forte et al., 2017; Wilson et al., 2011).

Deleted: s



216

217 **Figure 2** : Graphical summary of the model development. Flowchart made with *diagrams.net*.

Formatted: Font: Italic

218 3. Material and methods

219 **Figure 2** summarises the conceptual steps of our methodology. The aim is to capture vegetation
 220 impact from multi-spectral satellite images and train a ML model to explain it as a function of
 221 covariates describing hazard and vulnerability. We detail the successive steps of this
 222 methodology, from the quantification of vegetation impact (Section 3.1) and covariates (Section
 223 3.2) to the development, application and interpretation of the ML model (Section 3.3).
 224 Throughout the paper, we refer to metrics of vegetation impact as the *target variable*, whereas
 225 *feature* is used as a synonym for *co-variate* and/or *explanatory variable*, and *instance* as a
 226 synonym for a geographic *point*.

Deleted: Figure 2

Deleted: new

Deleted: to investigate the effects of tephra on vegetation using big EO data

Deleted: train a ML model to

Deleted: inferred

Deleted: s

Deleted: -Error! Reference source not found.

236 3.1. Quantifying vegetation impact from remote sensing data

237 *In situ* assessment of vegetation (including crops) impact is typically quantified using various
238 metrics ~~defined~~, depending on the purpose (e.g., percentage of destroyed vegetation or yield
239 loss; **Table 1**). We use the *Enhanced Vegetation Index* (EVI; Huete et al., 2002) as a remote
240 sensing-based proxy for biomass production (Kong et al., 2019; Poortinga et al., 2018), and
241 consider *impact* as a negative deviation of the post-eruption EVI signal. The EVI is retrieved
242 from MODIS imagery (i.e., the MYD13Q1 and MOD13Q1 V6 products) generated every 16
243 days at a spatial resolution of 250 m. This MODIS image collection was processed on GEE.

244 3.1.1. Temporal smoothing

245 The MODIS EVI image collection is temporally smoothed using the median pixel value over
246 consecutive time steps ~~(represented by the j index in Equation 1)~~. ~~We test here two-time~~
247 ~~windows of 1 and 3 months using the eruption date as a reference point.~~ This approach to
248 temporal smoothing, used to reduce artefacts, was selected over filtering-based (e.g., Savitski-
249 Golay filters) or non-parametric statistical (e.g., double logistic function) methods for two main
250 reasons. Firstly, these methods are sensitive to the density and the signal-to-noise ratio of the
251 time series (Cai et al., 2017; Li et al., 2021). As volcanoes are vast topographic edifices,
252 frequent clouds in their vicinity makes the application of such algorithms unstable and
253 unreliable. Secondly, we focus on the impacts occurring at a medium-term rather than in the
254 immediate aftermath of an eruption, where a Vegetation Index (VI) can capture signals that do
255 not record impact (e.g., increase in soil brightness due to tephra deposit). As a result, the median
256 value over a given time window presents the most stable and conservative smoothing method
257 around volcanoes.

258 3.1.2. *Anomaly quantification*

259 Multiple approaches have been developed to quantify VI *anomalies* ~~for purposes ranging from~~
260 early warning (e.g. Asoka and Mishra, 2015; Meroni et al., 2019; Rembold et al., 2019) to

Deleted: ,

Deleted: Table 1

Moved (insertion) [1]

Formatted: Font: Italic

Deleted: ¶

Moved up [1]: We test here two-time windows of 1 and 3 months using the eruption date as a reference point.¶

Deleted: *Anomaly quantification*

Deleted: with

Deleted: various

270 index-based parametric insurance (e.g. Martín-Sotoca et al., 2019). VI anomalies have also been
 271 used to monitor vegetation recovery after natural hazards (e.g. fires, Bright et al., 2019; volcanic
 272 ashfall, De Schutter et al., 2015), cropping intensities (e.g. Liu et al., 2020), long term land
 273 degradation (Gonzalez-Roglich et al., 2019) or changes in vegetation dynamics (Kalisa et al.,
 274 2019). We adapt the approach of Poortinga et al. (2018) as a proxy for impact of volcanic ash
 275 on vegetation, hereafter named Cumulative Difference Index (CDI). The CDI is computed as:

$$CDI_{i,t} = \sum_{j \in N_t} VI_{i,j,k} - \overline{VI}_{i,j}$$

277 Equation 1

278 where $CDI_{i,t}$ is the CDI value for pixel i for consecutive j values after the eruption up to time
 279 t . $VI_{i,j,k}$ is the median VI value for pixel i at a post-eruption period j in year k . N_t is a set of
 280 post-eruption periods that includes all j, k indices up to a time t and $\overline{VI}_{i,j}$ is the long-term VI
 281 mean over the baseline (averaged over 5 years prior to eruption for pixel i and period j). VI is
 282 the vegetation index (here, EVI) and j is an arbitrary time window, referring to a subset of a
 283 year. Here, j considers a 1–3-month period and the baseline considers 5 years of pre-eruption
 284 conditions. For the 2011 eruption of CC, the first CDI value (i.e., $j=1, k=1, t=1$) is simply the
 285 difference between the median VI value for Apr-Jun 2011 and the average of all Apr-Jun VI
 286 values in the period 2006-2010. The second CDI value would sum the differences over the set
 287 N_2 (i.e., $j=1,2, k=1, t=2$).

288 Whilst most remote sensing indices rely on ratios of pre/post conditions to define a relative
 289 anomaly (e.g., Hope et al., 2012; see section 3.2.2), the CDI relies on an absolute difference. It
 290 is important to note that therefore, by definition, pixels with high EVI values will result in larger
 291 CDI changes. However, the temporal evolution of the CDI offers a new approach to capture

Deleted: or

Deleted: j
 Deleted: k
 Deleted: t
 Deleted: $=1$
 Deleted: t
 Deleted: j/k

Formatted: Font: Italic
 Deleted: during the time period j for year k
 Deleted: j/k
 Deleted: during the time period
 Deleted: j
 Formatted: Subscript
 Deleted: for year k
 Formatted: Font: Italic
 Formatted: Font: Italic
 Formatted: Font: Italic
 Formatted: Font: Italic
 Formatted: Font: Italic
 Formatted: Font: Italic

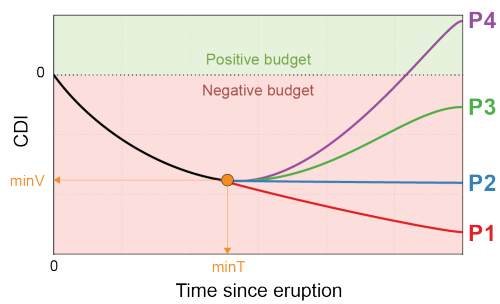
Formatted: Font: Italic
 Formatted: Font: Italic, Subscript
 Formatted: Font: Italic
 Formatted: Font: Italic
 Formatted: Font: Italic
 Formatted: Font: Italic

Deleted: The
 Deleted: is used as
 Deleted: the metric for

307 impact and recovery. **Figure 3** illustrates idealized profiles that the CDI can adopt through time.
 308 Following **Equation 1**, a scenario where the CDI gradient remains negative implies that post-
 309 eruption conditions are persistently lower than the baseline (i.e., P1 in **Figure 3**). A CDI
 310 flattening and reaching a zero gradient indicates a return to pre-eruption conditions (P2 in
 311 **Figure 3**). If the gradient of the CDI slope becomes positive after the inflection point, the post-
 312 eruption biomass production has exceeded pre-eruption conditions. If the CDI curve flattens at
 313 a negative CDI value, the total loss in biomass due to the eruption has been partly compensated
 314 by a temporary increase (P3 in **Figure 3**). Should the absolute CDI value become positive, the
 315 total biomass loss caused by the eruption has been either compensated or exceeded by the gains
 316 (P4 in **Figure 3**). The purpose of the model is to explore conditions explaining the magnitude
 317 of impact (i.e., $minV$ in **Figure 3**) and the duration to reach it (i.e., $minT$ in **Figure 3**). The shape
 318 of the CDI curve after reaching $minV$ is not considered here, and $minV$ for the case of P1 in
 319 **Figure 3** is the minimum value reached after 5 years post-eruption.

Deleted: Figure 3
 Deleted: Equation 1
 Deleted: where CDI_{ijk} remains
 Deleted: negative CDI slope,
 Deleted: Figure 3
 Deleted: Figure 3
 Deleted: Figure 3
 Deleted: Figure 3
 Deleted: Figure 3
 Deleted: Figure 3
 Deleted: Figure 3
 Deleted: Figure 3

320



321

322 **Figure 3:** Illustration of various possible CDI profiles through time. The x axis represents t in **Equation 1**. $minV$
 323 represents the minimum CDI value reached by a CDI profile and $minT$ the duration after which $minV$ has been
 324 reached. P1 represents a scenario with a permanent degradation of the EVI. P2 represents a scenario where post-
 325 eruption conditions have returned and remain equal to pre-eruption conditions. P3 represents a scenario where
 326 post-eruption conditions have returned and temporarily exceeded pre-eruption conditions without compensating

338 for the deficit caused by the eruption. P4 is similar to P3, but with post-eruption conditions sufficiently persisting
339 to compensate and exceed the deficit caused by the eruption.

340 **Table 2** : Summary of variables used in the model.

341 3.2. Model features

342 Co-variables used in the model to predict the impact (**Table 2**) were chosen to capture the
343 relevant hazard and vulnerability parameters identified from the literature (Section 2.1). Most
344 datasets are natively available on GEE, and others have been manually uploaded as assets. Note
345 that the original covariate dataset contained ~300 features. Here we present the final set of
346 variables identified based on i) a minimum degree of multicollinearity assessed during the
347 exploratory data analysis phase and ii) iterations of the process of model optimisation and
348 computation of feature importance described in section 3.4.3 that allowed identifying and
349 retaining the most informative variables.

350 **Table 3** : Initial parameters to the Fall3D runs. For the Suzuki plume model, A and λ are the shape factor
351 controlling the mass distribution described by Pfeiffer et al. (2005), where $\lambda=2$ results in more mass distributed in
352 the lower portion of the plume. The *FPlume* approach (Folch et al., 2016) was solved for mass flow rate (MFR,
353 Degruyter and Bonadonna, 2012). Two total grain-size distributions (TGSD) were tested including a field-based
354 Gaussian ($Md \Phi$ and $\sigma \Phi$ of 1.7 and 3.1, respectively; Bonadonna et al., 2015) and a model-based Bi-Weibull
355 (modes at -3.13 and 4.69 Φ with respective shape factors of 0.73 and 1.1 Φ and a mixing factor of 0.64; Costa et
356 al., 2016, Folch et al., 2021) distribution.

357 3.2.1. Deposit properties

358 Deposit thickness and grain-size distribution are the two of the main physical aspects
359 controlling the direct impact of ashfall on vegetation (Jenkins et al., 2015). Since available
360 isopach maps represent only deposit thickness, we reconstructed the grainsize distribution of
361 the deposit associated with the June 4-30 2011 phase of the CC2011 eruption using Fall3D
362 v8.0.1 (Folch et al., 2021). The model was initialised using hourly atmospheric conditions
363 retrieved from the European Centre for Medium-Range Weather Forecasts (ECMWF) ERA5
364 dataset (Hersbach et al., 2020) and daily mean plume heights reported by Collini et al. (2013).

Deleted: Table 2

Deleted: are

Deleted: ed

Deleted: relations

Deleted: in an

Deleted: an

Deleted: d

Deleted: (

Deleted: s

Deleted: e.g.,

375 We tested several modelling schemes (Table 3) and compared the outputs against the isopach
376 in Figure 1a. For this, isopachs were interpolated using a generalised additive model and
377 converted to maps of tephra accumulation using a constant deposit density. We tested densities
378 of 1000, 2000 and 2200 kg/m² to provide a range of tephra thicknesses for each point. The
379 Fall3D NetCDF output was converted to a multiband geotif with each band containing mass
380 loads for different size fractions. Size fractions computed by Fall3D were grouped into lapilli
381 (2–64 mm), coarse ash (1-0.25 mm) and fine ash (<0.25 mm). The geotif was uploaded as an
382 asset to GEE.

383 3.2.2. Climate

384 Atmospheric data were obtained from GEE using the ERA5 Land monthly averaged climate
385 dataset (Hersbach et al., 2020), which provides a global reanalysis of climate variables since
386 1981 at a spatial resolution of 0.1 x 0.1°. As the nature of the adopted ML model does not allow
387 for using time series as co-variates (see Section 3.4), we instead retrieve the total precipitation
388 and the surface air temperature and compute their mean over 1, 2, 3, 6 and 12 months before
389 the eruption. Each variable is considered both as raw values and anomalies computed as the
390 Stand Regeneration Index (SRI; Hope et al., 2012). As for CDI, we used a 5-years pre-eruption
391 baseline and normalized the closest pre-eruption value $V_{i,j,k}$ by the mean value over the same
392 period in the baseline $V_{i,j}$:

$$393 \quad SRI_{i,j,k} = \frac{V_{i,j,k}}{V_{i,j}}$$

394 Equation 2

395 For instance, a 3-months precipitation anomaly <1 suggests that the trimester before the
396 eruption was characterized by relatively lower rainfall compared to the same period of the year
397 in the 5-years baseline. By considering both raw values and anomalies, we explore the relevance

Deleted: Table 3

Deleted: Figure 1

Deleted: T

Deleted: were retrieved

Deleted: computed

Deleted: included

404 of each variable and potential pre-existing climatic stresses whilst also investigating what time
405 windows are relevant for vegetation impact. The model also includes the wind velocity at the
406 time of the eruption from the ERA5 Land dataset.

407 In addition to atmospheric variables, the model includes the updated 1-km version of the
408 Köppen-Geiger climate classification by Beck et al., (2018). The study area spans three of the
409 five main categories (*Arid*, *Warm temperate* and *Polar*), with two sub-types of the *Arid* (i.e.
410 *Desert – hot arid* and *Steppe – hot arid*) and four sub-types of the *Warm temperate* (*fully humid*
411 *– warm summer*, *fully humid – cold summer*, *summer dry – warm summer*, *summer dry – cool*
412 *summer*).

413 3.2.3. Terrain

414 Terrain data were obtained from the Shuttle Radar Topography Mission (SRTM; Farr et al.,
415 2007) using the NASA’s SRTM V3 product at a resolution of ~30 m. Elevation, slope, aspect,
416 eastness and northness (*sine* and *cosine* of aspect, respectively) were retrieved from GEE and
417 used as features.

418 3.2.4. Landcover

419 Landcover was obtained from Copernicus Global Land Service (CGLS) Dynamic Land Cover
420 map (CGLS-LC1000, Buchhorn et al., 2020), available on GEE at a spatial resolution of 100 m
421 yearly from 2015-2019. The landcover type is retrieved from the *discrete_classification* band
422 for the closest year to the eruption (here 2015, acknowledging that the 2015 dataset possibly
423 includes a long-term change in landcover caused by the 2011 eruption). To test the impact of
424 tephra on various types of vegetation, we extracted the *Cultivated and managed*
425 *vegetation/agriculture* class as a proxy for cropland and the *Shrubs*, *Sparse* and *Herbaceous*
426 *vegetation* classes (i.e., values 40, 20, 60 and 30, respectively). In addition, we extracted a
427 composite *Forest* class comprising all classes tagged with *Forest*. In the study area, present

Deleted: (

Deleted: Beck et al., (2018)'s updated 1-km version of the Köppen-Geiger climate classification

Deleted: A One Hot Encoding procedure was applied to this dataset to transform categorical labels into the numerical values required by most ML algorithms.

Formatted

Deleted:).

435 forest classes include *Evergreen broad leaf*, both *Closed* (112) and *Open* (122), *Deciduous*
436 *broad leaf*, both *Closed* (114) and *Open* (124) as well as *Closed forest, mixed* (115) and *Forest,*
437 *not matching any of the other definitions* (116 and 126).^v

Deleted: As for the climate classification, a *One Hot Encoding* procedure was applied to landcover classes.

438 3.3. Point sampling

439 In the study area, the vegetated landcover classes defined above account for 96% of the total
440 landcover, with the classes *Shrubs* (38%), *Sparse* (26%) and *Herbaceous* (17%) dominating the
441 total count. The *Forest* class (17%) dominates the Andean part of the study area whereas crops
442 represent about 1% of the region. 5000 instances were randomly sampled for each landcover
443 class. The target variables and covariates for all points were downloaded from GEE and stored
444 as a *GeoPandas* dataframe in Python.

445 3.4. Setting up the machine learning model

446 We developed an interpretable ML model able to process big EO data to identify the most
447 important variables and how they interact to cause the impact on vegetation. This amounts to a
448 (supervised learning) regression task; the EO data, for training and testing, include the
449 environmental, atmospheric, and geophysical features described above, as well as the target
450 variables consisting in the impact metrics. The main objective is to investigate and describe the
451 nature of the processes, performing out-of-sample predictions (*i.e.* **model generalisation**) is
452 outside of the scope of this paper. This section introduces the ML algorithm, its optimisation
453 and its interpretation processes. All computations are performed using *Python 3.9* on the *Gekko*
454 cluster of NTU's *Asian School of the Environment*, both using CPUs and GPUs.

455 3.4.1. ML algorithm

456 The main modelling challenge is to approximate complex functions mapping both *minV* and
457 *minT* to the various investigated features. Decision trees and related methods form a general
458 class of models suitable for such regression tasks. We opt for Gradient Boosted trees, a category

461 of decision trees that use an ensemble of so-called weak learners built sequentially to improve
462 prediction accuracy (Müller and Guido, 2015) [and capable of handling multicollinearity](#) (Cheng
463 et al., 2018). Gradient Boosted trees have successfully been applied on EO problems (e.g.,
464 [Hengl et al., 2017](#)). Here, we used the *XGBoost v.1.4.2* library, which provides an optimised
465 and distributed implementation of gradient boosted trees (Chen and Guestrin, 2016).

466 3.4.2. Hyperparameter optimisation

467 Gradient-Boosted trees rely on a range of hyperparameters governing the model's bias-variance
468 trade-off. Selected hyperparameters (Section 4.4.1) were tuned by minimising the out-of-
469 sample mean absolute error (MAE) computed through a 5-fold cross-validation scheme using
470 *Scikit-learn's RepeatedKFold* and 10,000 trees. We used the *Optuna* library (Akiba et al., 2019)
471 optimised on a single GPU.

472 3.4.3. Model interpretation

473 Gradient-Boosted trees can accommodate non-linear effects and interactions but, as for many
474 modern ML algorithms, come at the cost of limited interpretability. Model-agnostic
475 interpretation methods shedding light on black-box models are actively being developed and,
476 when applied on big EO data, provide a novel framework to identify and constrain the processes
477 driving changes through time in Earth Sciences (Batunacun et al., 2021; He et al., 2020; Sulova
478 and Arsanjani, 2021). Amongst these, the Shapley additive explanations (SHAP) method of
479 Lundberg et al., (2020), based on Shapley values (Shapley, 1956) and coalitional game theory,
480 decomposes any prediction from a given model as a sum of the individual effects from each
481 variable (Molnar, 2021). The method computes SHAP values, which quantify how a given
482 feature act to change a model's mean prediction. We use here SHAP values to identify drivers
483 of vegetation vulnerability in two ways. Firstly, the mean absolute SHAP value of a variable
484 across all instances indicates a relative importance amongst all features. Secondly, individual
485 SHAP values for a given feature and all instances provide insights into how a feature's value

486 influences predictions. As ~~this study does not attempt to perform out-of-sample predictions,~~
487 SHAP values are computed on the full dataset. We use the *TreeExplainer* method of the SHAP
488 library (Lundberg et al., 2020) to explain XGBoost’s prediction.

Deleted: generalisation is not the main objective of this study

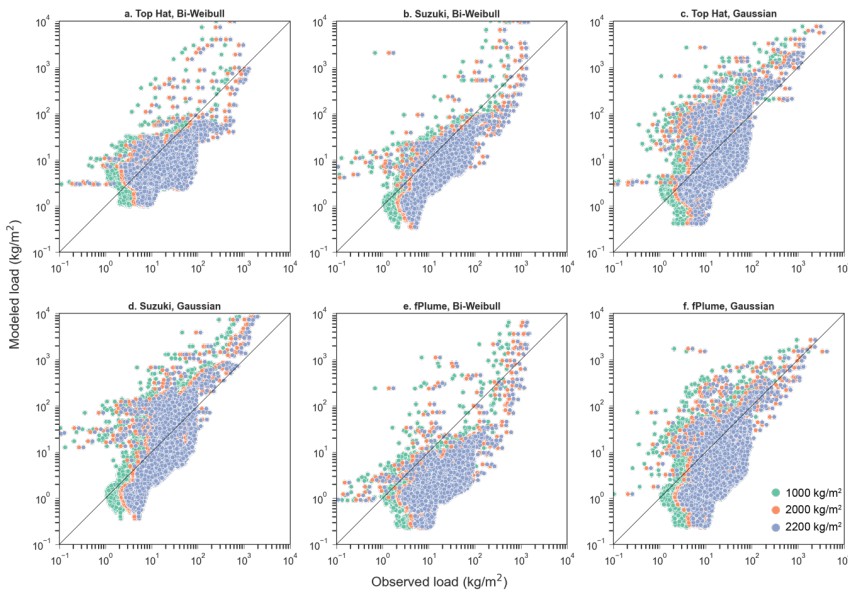
489 Unlike SHAP values, *permutation feature importance* ranks features based on their direct
490 impact on model performance (Breiman, 2001; Fisher et al., 2019). We use it as a
491 complementary approach to SHAP values. Permutation importance is also computed on the full
492 dataset using *Scikit-learn*’s *permutation_importance* function using 10 permutations of each
493 variable and computing the change in the coefficient of determination R^2 .

494 3.4.4. Modeling scheme

495 A model is trained separately for each landcover class defined in Section 3.3, with one
496 additional model trained on all landcover classes jointly and using the landcover class as a
497 feature. Since *XGBoost* does not support multi-output regressions, each dataset is used as an
498 input for two models trained using either *minV* or *minT* as a target variable (**Figure 3**). To
499 include some dependence between the two impact metrics, the model predicting *minV* is trained
500 with *minT* removed from the features, whereas the model predicting *minT* is trained with *minV*
501 in the list of features.

Deleted: Figure 3

504 **4. Results**



505

506 **Figure 4** : Relationship between the tephra accumulation modelled with **Fall3D** and inferred from isopach for the
507 various modelling schemes (**Table 3**). Colours consider various densities used to convert deposit thickness to mass
508 loads. Figure sub-labels follow **Table 3**. The black line shows a hypothetical 1:1 relationship.

Deleted: Fall3d
Deleted: Table 3
Deleted: Table 3

509 **4.1. Deposit reconstruction**

510 To select the best **Fall3D** run shown in **Table 3**, 10,000 points were randomly sampled in space
511 and used to retrieve both the modelled tephra load and the thickness obtained from interpolated
512 isopach (**Figure 4**). Although all model runs are capturing the general trend, mismatches can
513 be attributed to modelling issues (e.g., limitation in describing sedimentation from the plume
514 margin or aggregation processes; Bagheri et al., 2016; Poulidis et al., 2021) and isopach
515 interpolation using a bulk density. In the perspective of these limitations, we adopted run *b* (i.e.,
516 Suzuki plume model with a bi-Weibull grain-size distribution; **Table 3**) as it generally shows a
517 minimum spread across the 1:1 line and provides a conservative scenario (**Figure 4**). **Figure 5**.

Deleted: Fall3d
Deleted: Table 3

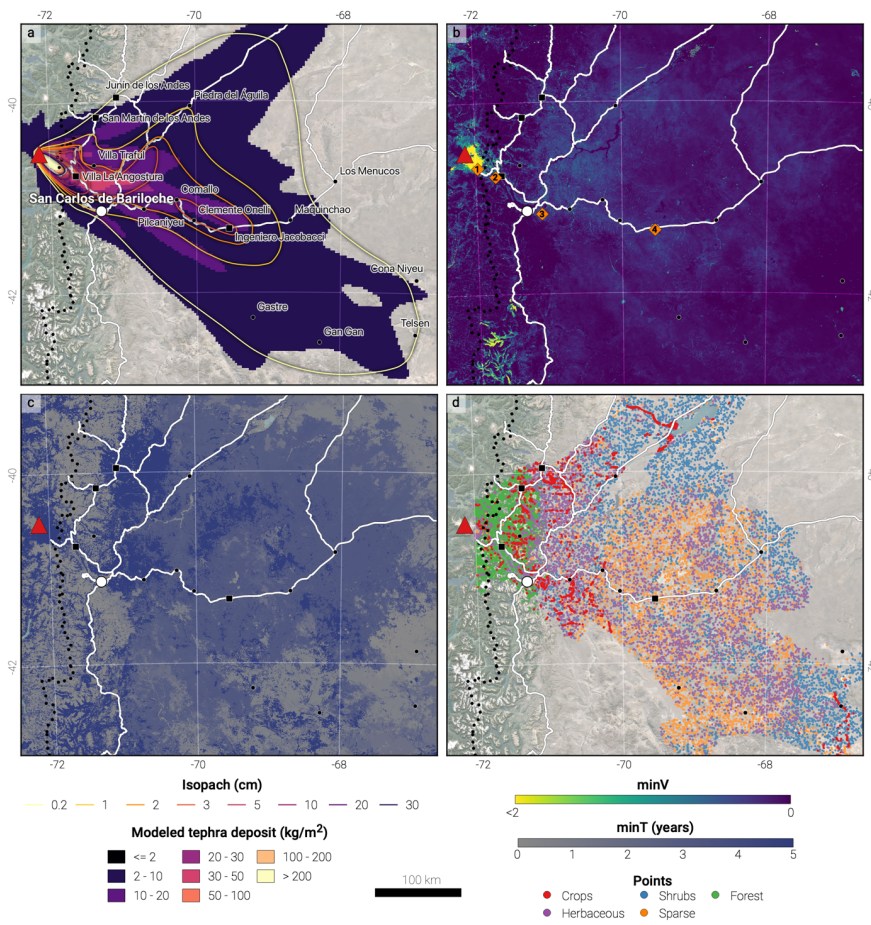
Deleted: Figure 4

Deleted: Table 3

Deleted: Figure 4

Deleted: Figure 5

527 a compares the modelled load for the selected run with the isopach. The model captures both
 528 the general extend of the deposit as well as the various lobes generated as a function of variable
 529 wind conditions throughout the eruptive phase.



530

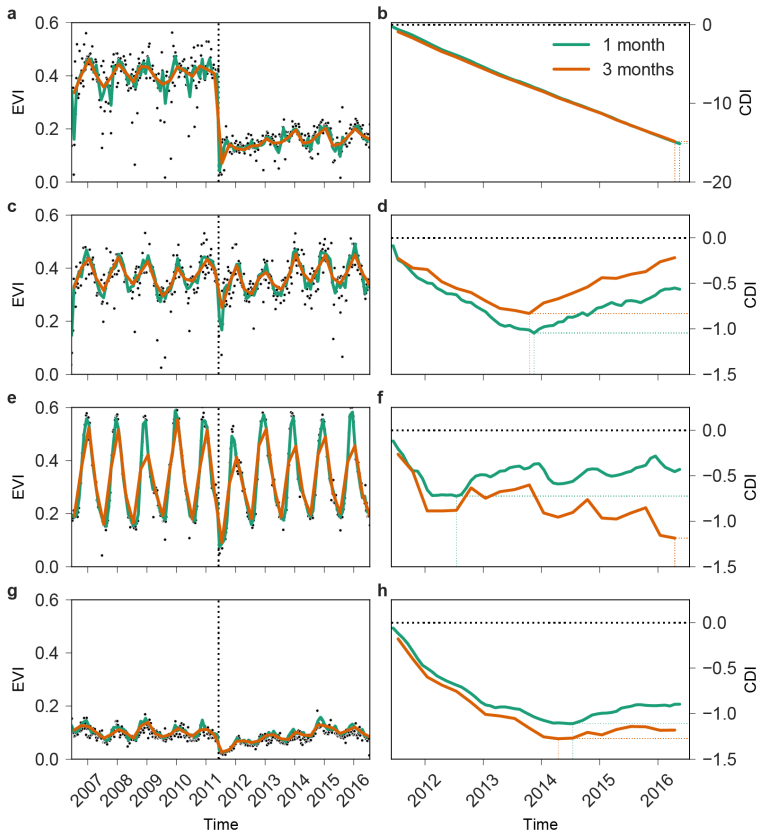
531 **Figure 5** : a Modelled load using **Fall3D** run b (kg/m^2 ; **Table 3**) overlain with isopach (cm). b Spatial distribution
 532 of *minV*. Numbered orange diamonds are referenced in the text. c Spatial distribution of *minT*. d Dataset of points
 533 sampled in GEE coloured by their landcover class. When not specified, legend items follow **Figure 1**. Background
 534 is © Google Map 2022.

535

Deleted: Fall3d

Deleted: Table 3

Deleted: Figure 1



539

540 **Figure 6** : Time series of EVI (a, c, e, g) and monthly CDI (b, d, f, h) for the four points described in Section 4.2
 541 and located in [Figure 5](#). Black dots are raw (i.e., non-composited) MODIS data whereas green and orange lines
 542 are composited collections using a kernel of 1 and 3 months, respectively, as described in Section 3.1. On the left
 543 plots, the vertical black dashed line indicates eruption time. On the right plots, the horizontal black dashed line
 544 indicates a neutral budget ([Figure 3](#)). Coloured dotted lines indicate the location of $minV$ and $minT$.

545 **4.2. Anomaly quantification**

546 [Figure 6](#) shows an illustration of time series of EVI and associated monthly CDI for four
 547 representative points in the study area ([Figure 5, b](#)) chosen to represent the spread in tephra
 548 accumulation and vegetation/climate types, and using compositing windows of 1 (green) and 3
 549 (orange) months. Seasonal EVI patterns, with high values in the summer reflecting active

Deleted: Figure 5

Deleted: Figure 3

Deleted: Figure 6

Deleted: Figure 5

554 growth and low values in the winter reflecting plant dormancy, indicate that the eruption
555 occurred during a period of low growth (Elissondo et al., 2016). Point 1 (Figure 6, a, b), located
556 23 km southeast of the vent, is characterized by herbaceous vegetation and a modelled tephra
557 load of 330 kg/m² (thicknesses of 165–330 mm when converted with deposit densities of 2000
558 and 1000 kg/m³, respectively). The sharp drop in EVI after the eruption and the following
559 persistent lower values compared to the pre-eruption baseline translate into a CDI profile
560 showing a negative slope, which indicates that the system did not return to pre-eruptive
561 conditions. This observation agrees with existing DDS (Table 1), where accumulations ≥150
562 mm result in substantial vegetation destruction. Point 2, located 45 km southeast of the vent
563 and 7 km from Villa La Angostura consists of closed, evergreen broadleaf forest. With 40 kg/m²
564 of tephra accumulation (thickness of 20–40 mm for the same densities as Point 1), EVI values
565 show a slight decrease compared to pre-eruption conditions lasting for a couple of years, after
566 which a general trend is observed leading to larger EVI values than the baseline (Figure 6, c).
567 This translates into CDI profiles showing a negative trend for two years after the eruption, after
568 which a positive trend indicates better conditions compared to the baseline (Figure 6, d). When
569 compared to existing DDS for forestry (Table 1), the modelled thickness spans damage classes
570 0–3, ranging from no impact to minor productivity loss. Point 3 is 112 km from the vent in the
571 vicinity of San Carlos de Bariloche. Classified as crops by the CGLS landcover and looking
572 like pastoral grazing fields from high resolution satellite imagery, it was affected by 7 kg/m² of
573 tephra (thickness of 3.5–7 mm; damage classes 0–3; Table 1). Both compositing time windows
574 show a reduction in EVI values for at least one season after the eruption (Figure 6, e, f). Finally,
575 Point 4 is located 240 km southeast of the vent close to Ingeniero Jacobbaci and was affected
576 by 10 kg/m² of tephra (i.e. 5–10 mm). Classified as herbaceous vegetation in the CGLS dataset
577 but looking like farmland with a mixture of pasture and crops on high-resolution satellite

Deleted: Figure 6

Deleted: Table 1

Deleted: Figure 6

Deleted: Figure 6

Deleted: Table 1

Deleted: Table 1

Deleted: , which translates to a local CDI minimum about a year after the eruption

Deleted: Figure 6

587 imagery, both EVI and CDI profiles indicate a return to pre-eruption conditions after ~3 years,
588 after which a positive CDI slope indicates temporary better conditions (Figure 6 g, h).

Deleted: Figure 6

589 Figure 6 illustrates the differences in quantifying $minV$ and $minT$ when using time windows of
590 1 and 3 months in Equation 1. A 1-month window closely follows local trends and results in
591 irregular CDI curves, whereas a 3-months window over-smooths local variations. Although
592 both approaches commonly result in similar results, Point 3 illustrates how the two windows
593 can induce different interpretations. We adopt a 3-months kernel for two main reasons. Firstly,
594 the visual comparison of the spatial distribution of $minV$ and $minT$ on a map shows that such
595 differences occur locally whilst preserving the general spatial distribution. Secondly, points
596 displayed in Figure 6 are not heavily affected by cloud coverage, and the 1-month kernel does
597 not reflect the typical effects that clouds can induce when using such a small compositing time
598 window (e.g., sparse time-series, artefacts, etc.). This is generally not the case, either around
599 Cordon Caulle volcano where the region closer to the vent suffers too much cloud coverage to
600 be resolved by a 1-month kernel, or around most volcanoes around the world where large and
601 high edifices are often cloudy. Therefore, the 3-months kernel provides a more conservative
602 approach and enables reproducibility to other case studies.

Deleted: Figure 6

Deleted: Equation 1

Deleted: Figure 6

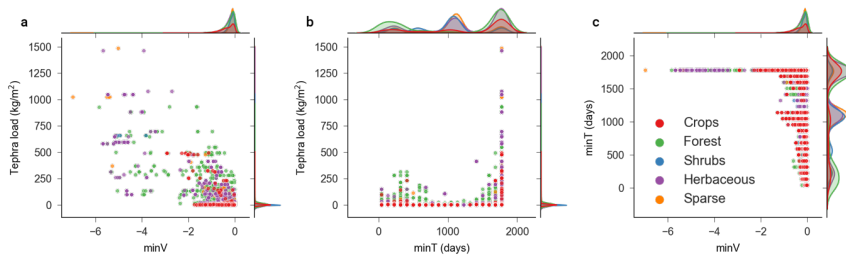
603 4.3. Impact mapping

604 Figure 5 b displays the spatial distribution of $minV$ in the study area. The region with the
605 minimum $minV$ value extends up to 25 km southeast of the vent and corresponds to
606 accumulations of ~550 kg/m². Although conspicuous, it is impossible to unequivocally attribute
607 this impact to tephra fallout in proximal area where other hazards can occur (e.g., pyroclastic
608 density currents, lahars). Except for this region, the impact within the first 80 km east of the
609 vent is relatively limited, beyond which a sharp, north-south oriented decrease in $minV$ values
610 occur. This rapid change corresponds to a change in rainfall amount, a transition from well-

Deleted: Figure 5

616 developed andosols to very weakly-developed regosols and a region dominated by forests to
 617 one dominated by shrubs and herbaceous vegetation (Figure 1; Section 2.2). In this region,
 618 minimum $minV$ values are ~ -0.5 and the spatial distribution of $minV$ reflects the spatial
 619 distribution of tephra fallout. Negative $minV$ values extend eastwards beyond the town of Los
 620 Menucos, suggesting that impact occurred with accumulations $\leq 2 \text{ kg/m}^2$. Due to the use of a 3-
 621 months kernel, $minT$ is a discrete rather than a continuous dataset (i.e., a $minT$ value of 4.5
 622 months suggests that $minV$ was reached between 3–6 months after eruption onset). The spatial
 623 distribution of $minT$ (Figure 5c) generally reflects $minV$ and the pattern of tephra accumulation.
 624 Note that artefacts related to non-vegetated areas are ignored (e.g., bare rock and snow-covered
 625 mountains in the S).

626 Figure 5d shows the distribution of sampled points by landcover and selected relationships are
 627 plotted in Figure 7. Although Figure 7a displays a general negative relationship between $minV$
 628 and the tephra load, a simple linear relationship fails to accurately capture the variability of
 629 impact. For $minT$, Figure 7b and c show how $minT$ is distributed around three main modes of
 630 tephra load and $minV$. Landcover classes that are most impacted by long $minT$ values are Forests
 631 and Herbaceous, which are the two classes the most exposed to heavy loads (Figure 5). Plotting
 632 $minT$ shows a distribution centred around three modes of about 400, 1000 and 1700 days
 633 (Figure 7b). High $minV$ and tephra loads generally result in larger $minT$ values,



634

Deleted: Figure 1

Deleted: Figure 5

Deleted: Figure 5

Deleted: Figure 7

Deleted: Figure 7

Deleted: Figure 7

Deleted: Figure 5

Deleted: Figure 7

Deleted: No clear relationship appears between

Deleted: $minT$

Deleted: a

Deleted: either $minV$ or

Deleted: .

648 **Figure 7** : Relationship between **a** *minV* and the total tephra load, **b** *minT* and the total tephra load and **c** *minV* and
649 *minT* as a function of the landcover class. The marginal axes contain a kernel density estimate of the underlying
650 population for each landcover class. For readability all forest sub-groups are grouped.

651 4.4. ML model

652 **Table 4** : Summary of the trained models. The *Optimisation* columns group reports the hyperparameter values
653 obtained with the optimisation process. *Max depth is the maximum depth of each tree; ETA is the learning rate;*
654 *alpha and lambda are the L2 regularisation terms; Min Child Weight controls the minimum number of observations*
655 *required in each node. See the XGBoost documentation for further details* (Chen and Guestrin, 2016). The *Model*
656 *metrics* columns group reports the mean absolute error (MAE) and the r^2 coefficients on both training and test
657 datasets. The mean and the standard deviation (Std) were obtained by 5-fold cross validation with three repeats.

658 4.4.1. Model performance

659 **Table 4** presents the results of the optimization of hyperparameters on the dataset shown in
660 **Figure 5**, d and the associated model metrics. The MAE and R^2 were computed on both training
661 and testing datasets using a cross-validation with five folds and three repeats. We compare
662 training and testing prediction error as an indication of the degree of overfitting of the model.
663 As expected, model metrics obtained on test datasets were lower than those using training data.
664 Based on the R^2 of the testing data and *minV*, models trained on all landcover classes and on
665 herbaceous vegetation performed well ($R^2 > 0.9$), followed by forests ($R^2 > 0.8$) and crops
666 ($R^2 > 0.7$). The particularly low R^2 value for sparse vegetation can be attributed to the presence
667 of <10% vegetated cover in this class, which is dominated by bare soil or rock. The R^2 values
668 of *minT* are consistently lower than those for *minV* and never exceed 0.6, which we partly
669 attribute to its discrete nature.

670 Overall, the comparison of error metrics between testing and training sets reveal that models
671 trained on the various datasets have various degrees of generalisation ability, with the caveat
672 that the validity of the insights provided by the different models should be considered in the
673 perspective of their respective performances. The broadest dataset considering all landcover
674 classes and *minV* results in high training (0.94) and testing (0.91) R^2 values. We use this good

Deleted: Table 4

Deleted: Figure 5

Deleted: Hyperparameters for all model runs generally showed a balance between parameters indicating a more (i.e., high values of alpha, lambda and min child weight) or less (i.e., high values of max depth and learning rate) conservative model. ...

682 performance and similarity between both values as an indication that the model is likely not
683 overfitting and yields good generalisation.

684 **Table 5** : Ranking of feature importance computed using mean absolute SHAP values and permutation importance
685 for all landcover class and impact metrics. A darker cell colour indicates a stronger importance. For each column,
686 the 3 most important features are in bold and the 10 most important features are in red.

687 4.4.2. Feature importance

688 **Table 5** summarizes feature importance for each landcover class using the mean absolute SHAP
689 value and permutation importance. Although some differences exist, both methods yield similar
690 results, thus implying that features that contribute the most to predictions (SHAP importance)
691 also improve the model's generalization error (permutation importance). Unless specified, this
692 section focuses on SHAP importance.

693 *EVI* and *elevation* are the two features that consistently rank in the top 10 of the most important
694 variables across impact and landcover. For *minT*, *minV* is the most important variable, which
695 suggests that both impact metrics are dependent. *EVI* ranks especially high, which indicates
696 that the mean *EVI* value computed over the year before the eruption provides an important
697 background level to the model. This result is a consequence of the cumulative sum of absolute
698 differences behind the CDI, which implies that pixels with higher *EVI* values are prone to larger
699 CDI impacts (section 3.1.1). The variable *Lapilli* is the most important for *minV* for all
700 landcover classes but crops (SHAP value) and sparse (permutation importance) and ranks high
701 when predicting *minT* for all and the forest landcover classes.

702 For forests, *minV* is best predicted, in decreasing order, by *lapilli*, *EVI* and *elevation*, which are
703 respectively a deposit, a proxy for a biotic and an abiotic parameter. Note that using permutation
704 importance instead of SHAP importance suggests that the 3rd most important variable is surface
705 temperature, which is correlated to *elevation*. In parallel, *minT* is driven by *minV*, *lapilli*,
706 *elevation* and *EVI*, which indicates that the duration of impact is dominantly proportional to the

Deleted: Table 5

708 magnitude of impact and the tephra load. In comparison, the *minV* of herbaceous vegetation is
709 controlled by lapilli, EVI and the 6-months precipitation, which indicates the same hierarchy
710 of importance of deposit, biotic and abiotic parameters as for forests, whereas *minT* is controlled
711 by *minV*, EVI, the 3-months precipitation and fine ash. Interestingly, this suggests that impact
712 duration does not primarily depend on any deposit variable, the most important of which (i.e.,
713 fine ash) is different to the parameter controlling the magnitude of impact (i.e., lapilli). As a
714 final example, no deposit property ranks in the top 3 variables controlling the *minV* values of
715 crops, which include climate, EVI and the 3-months precipitation anomaly. The first deposit
716 parameter, fine ash, ranks 4th, which indicates that the vulnerability of crops to ash fallout is
717 dominantly constrained by biotic and abiotic parameters. Fine ash ranks 5th for *minT*, which is
718 mainly driven by *minV*, EVI and the slope, and illustrate how abiotic parameters can potentially
719 dominantly control impact magnitude and duration.

720 4.4.3. SHAP dependence plots

721 SHAP dependence plots (Fig. 8) display, for each instance in the dataset (i.e., a point in [Figure](#)
722 [5, d](#)), the SHAP value of a given variable as a function of its actual value. For a given instance
723 and a given variable, a negative SHAP values implies that the variable contributed to reducing
724 the predicted value compared to the mean prediction of the model. Therefore, a negative SHAP
725 value for *minV* implies a contribution to *increase* the magnitude of impact, whereas a negative
726 SHAP value for *minT* implies a contribution to *decrease* the duration of impact.

727 Impact of deposit on *minV* predictions

728 [Figure 8, a](#) is the dependence plots for lapilli. With loads $\leq 60 \text{ kg/m}^2$ of lapilli, SHAP values
729 are contained within 0 ± 0.1 , but drastically drop for larger loads. Lapilli being dominantly
730 impacting the vicinity of the volcanic source, <4% of all instances are affected by
731 accumulations $>60 \text{ kg/m}^2$ with those areas dominantly consisting of forests with additional
732 vegetation classified as shrubs and herbaceous ([Figure 1, c](#)). Despite limited points, [Figure 8, a](#)

Deleted: , with additional biotic and abiotic controls

Deleted: (Amalds, 2013) This suggests that forests are potentially more resilient to moderate accumulations of ash and might rather be prone to direct, physical impact from heavy accumulations.

Deleted: Figure 5

Deleted: Figure 8

Formatted: English (UK)

Deleted: Figure 1

Deleted: Figure 8

742 suggests stepwise decreases in SHAP values for lapilli loads of ~60, 230 and 550 kg/m². Using
743 a deposit density of 1000 kg/m³, thicknesses of 60, 230 and 550 mm span the D1–D4 damage
744 states for forestry (Jenkins et al., 2014; [Table 1](#)). Using the pastoral class of [Table 1](#), as an
745 analogue for shrubs and herbaceous vegetation, these accumulations suggest that, for crops,
746 substantial to major land rehabilitation is required before recovery. These observations confirm
747 the relationships between *minV*, *minT* and the deposit load shown in [Figure 7](#); points affected
748 by high lapilli loads result in *minT* values larger than ~1300 days and an impact that persisted
749 for years after the eruption. These high impact metrics explain why lapilli is the most important
750 variable to predict *minV*. Lapilli is likely to cause a direct, physical impact from the high kinetic
751 energies (e.g., Blake et al., 2015; Osman et al., 2019), breakage from a static load and burial
752 (Arnalds, 2013; Ayris and Delmelle, 2012), which is captured as a strong anomaly by our
753 method and results as the most important variable. Plotting the dependence plot of lapilli for
754 the model trained on the generic forest landcover class ([Figure 8](#) b) indicates that the 2-months
755 precipitation anomaly contributes to further explaining the influence on the SHAP value, with
756 points with an anomaly <0.85 displaying lower SHAP values.

Deleted: Table 1

Formatted: Font: Not Bold

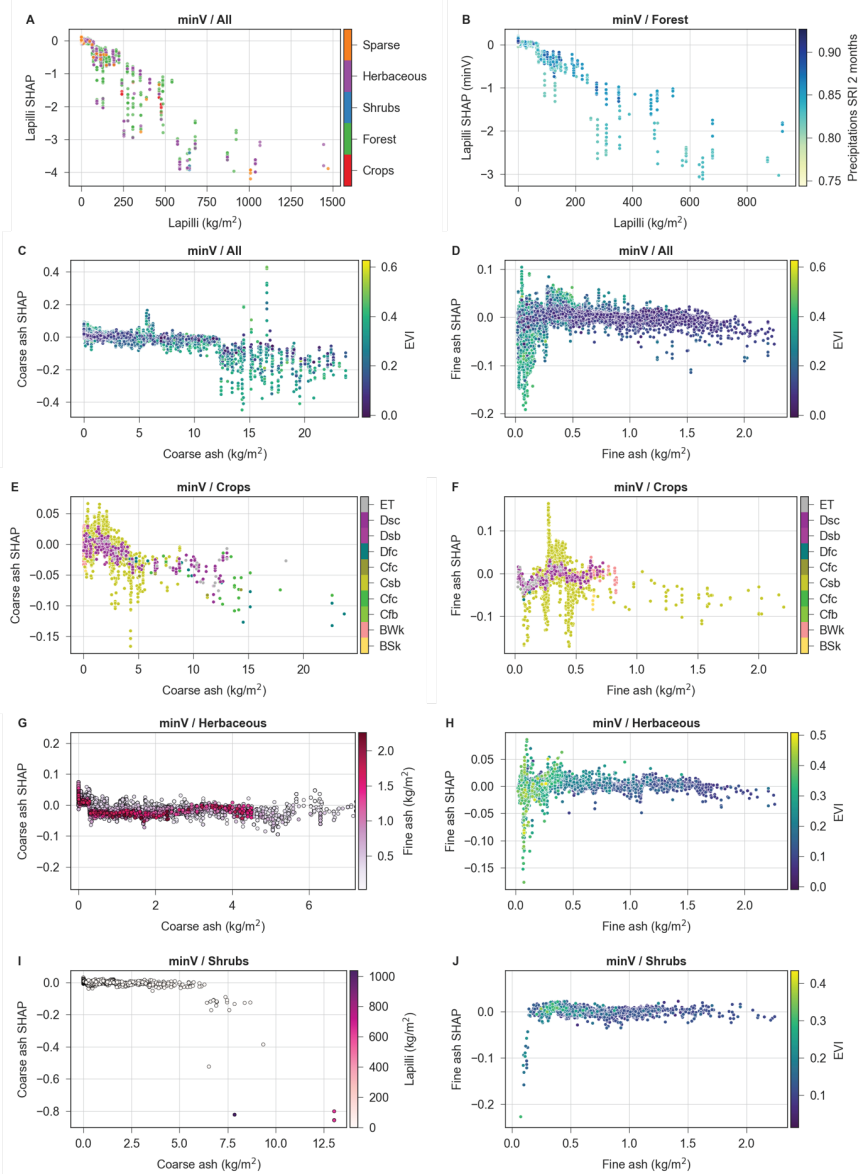
Deleted: Table 1

Formatted: Font: Not Bold

Formatted: Font: Not Bold

Deleted: Figure 7

Deleted: Figure 8



761

762 **Figure 8:** SHAP dependence plots illustrating the effect of deposit on the *minV* value predicted by the models for
 763 **a** lapilli using all landcover classes, **b** lapilli on the forest subclass and **c-j** coarse and fine ash for selected landcover
 764 classes. The hue of the points is related to additional explanatory variables. For **a**, **e** and **f**, the colour scheme
 765 follows [Figure 1](#). Negative SHAP values contribute to decreasing *minV* and therefore increase impact.

Deleted: Figure 1

767 Dependence plots for coarse and fine ash (Figure 8, c, d) display similar – although less
768 conspicuous – drops in SHAP values for accumulations of 12 and 1.7 kg/m², respectively, with
769 SHAP values on average one order of magnitude smaller than for lapilli. Considering that fine
770 deposits are denser than coarser ones, a density range of 1000–2000 results in thicknesses of 6–
771 12 and 0.9–1.7 mm for coarse and fine ash, respectively, which cover the D1–D3 damage
772 classes for Horticultural/Arable and Pastoral agriculture (Table 1). Note that these thicknesses
773 should be regarded as minimum values as we convert here individual size fractions to total
774 deposit thickness. Figure 8, e–j also shows the effect of ash for models trained on specific
775 landcover classes. For crops (Figure 8, e–f), coarse and fine ash are the 10th and the 4th most
776 important variables, respectively. Coarse ash seems to induce drops in SHAP values for loads
777 of 2, 4 and 10 kg/m². There is clearly an effect of fine ash on SHAP values but the oscillatory
778 pattern is difficult to explain for loads ≤0.5 kg/m², especially for the Csb climate class where
779 most crops are found (i.e., Warm temperate, summer dry, warm summer), and probably depends
780 on additional variables not accounted for in the model (e.g., geographic distribution of plant-
781 specific effects such as ash retention as a function of leaf morphology). Beyond 1 kg/m², SHAP
782 values are consistently negative. Coarse and fine ash are the 4th and the 14th most important
783 variables for *minV* for herbaceous vegetation. The coarse ash shows more negative SHAP
784 values when associated with fine ash. Fine ash is generally beneficial for herbaceous vegetation
785 with low EVI values (Figure 8, h). For herbaceous vegetation, the most negative SHAP values
786 are found for high-EVI with accumulations ≤1 kg/m². Incidentally, such accumulations also
787 correspond to the highest SHAP values. Since no co-variate satisfactorily explains this
788 contrasting behaviour, this is either due to a model artefact or to variables that are not accounted
789 for in the model. For shrubs (Figure 8, i–j), coarse and fine ash are respectively the 7th and 12th
790 most important variables. Coarse ash suggests a decrease in SHAP values for loads of ~6 kg/m²,

Deleted: Figure 8

Deleted: Table 1

Deleted: Figure 8

Deleted: Figure 8

Deleted: induces significant

Deleted: Figure 8

Deleted: The

Deleted: herbaceous vegetation for

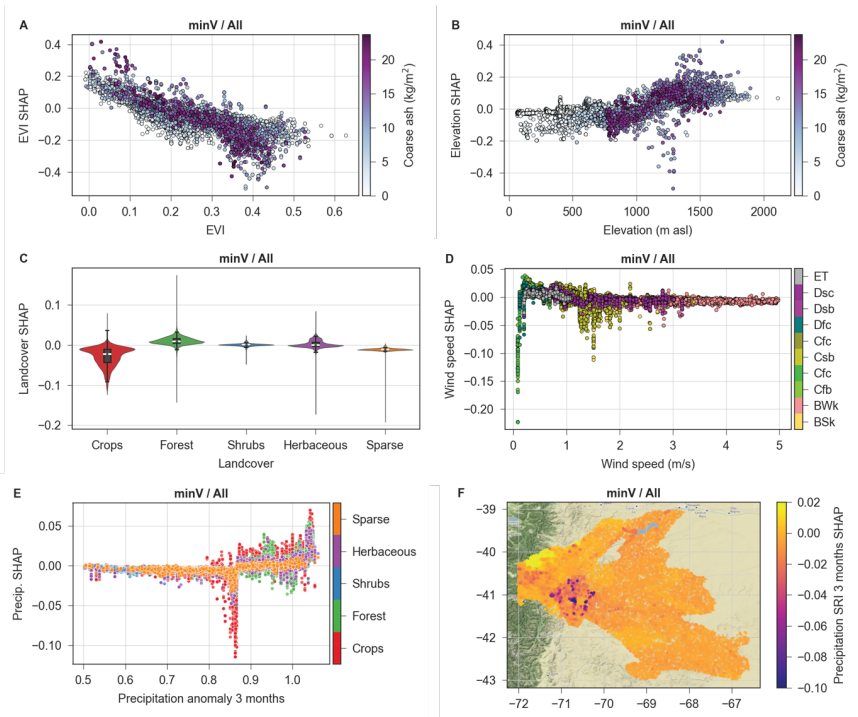
Deleted:

Deleted: and show both positive and negative behaviours

Deleted: Figure 8

Deleted: shows a sharp

803 beyond which the magnitude of the negative effect increases with the lapilli load. Fine ash
 804 doesn't show any trend or sharp break.



805
 806 **Figure 9:** a–e SHAP dependence plots illustrating the effect of various variables on the prediction of *minV*. a–b
 807 Effect of EVI (a) and elevation (b) on the SHAP value as a function of the coarse ash load. c Violin plot showing
 808 the distribution of SHAP values for each landcover class with a box-and-whisker plot overlain. d Effect of wind
 809 speed on the SHAP values as a function of climate. e Effect of the 3-months precipitation anomaly on the SHAP
 810 value as a function of landcover. f Spatial distribution of 3-months precipitation anomaly SHAP values. Map tiles
 811 by Stamen Design CC BY 3.0, map data © OpenStreetMap contributors.

812 **Impact of other features on the prediction of *minV***

813 **Figure 9**, shows SHAP dependence plots for variables other than the deposit. **Figure 9**, a
 814 confirms the importance of EVI on *minV*, where all points with EVI<0.1 result in positive
 815 SHAP values and all points with EVI>0.3 result in negative SHAP values. This observation is

Deleted: Figure 9

Deleted: Figure 9

818 partly a consequence of the use of [Equation 1](#), where the value of $V_{ijk} - \overline{V_{ij}}$ is generally larger
819 for higher EVI values. [Figure 9](#), a also suggest a dependence of this relationship on the load of
820 coarse ash, which slightly increases SHAP values for low EVI, but decreases them for higher
821 values. Elevation is the 3rd important feature for predicting $minV$ and shows a breakpoint at an
822 altitude of ~1000 m asl ([Figure 9](#), b), below which SHAP values are dominantly negative.
823 Above this elevation, SHAP values are generally positive, regardless of the intensity of ash
824 accumulation. Landcover, the 7th most important feature, indicates that crops dominantly
825 contribute to increasing impact in the model ([Figure 9](#), c). Sparse vegetation also has a negative
826 but less pronounced effect on SHAP values, whereas shrubs and herbaceous vegetations have
827 a neutral effect. The SHAP values of forests tend to reduce the impact, which corroborates the
828 higher resilience of trees to tephra fallout ([Table 1](#)). ,
829 Wind and precipitation partly control the residence time of ash on leaves and therefore the
830 impact (Ayrís and Delmelle, 2012). Although variables used here only consider pre-eruption
831 atmospheric conditions, they are indirectly used as indicators for post-eruption patterns. The
832 impact of wind speeds on SHAP values [suggests](#) breakpoints at 0.2 and 1.2 m/s. SHAP values
833 are strongly negative below 0.2 m/s, generally positive up to 1.2 m/s and generally negative
834 above ([Figure 9](#), d). This supports the idea that wind contributes to reducing the residence time
835 of ash on leaves, but the aeolian remobilization of ash at higher wind speeds can negatively
836 impact vegetation (e.g., Arnalds, 2013; Craig et al., 2016b; Elissondo et al., 2016; Wilson et al.,
837 2011). Although depending on additional parameters (e.g., surface roughness, ash properties,
838 soil humidity, rainfall intensity), an empirical value for onset of remobilization of 0.4 m/s has
839 been used in the literature and agrees with our results (e.g., Folch et al., 2014; Liu et al., 2014).
840 Leadbetter et al., (2012) observed that ash resuspension is suppressed if precipitation rates
841 exceed 0.01 mm/h, and our model indicates that most negative SHAP values occur for relatively
842 dry climates. The most important precipitation variable for predicting $minV$ with all landcover

Deleted: Equation 1

Deleted: Figure 9

Deleted: Figure 9

Deleted: Figure 9

Deleted: Table 1

Deleted:

Deleted: shows

Deleted: Figure 9

851 classes is the precipitation anomaly computed over 3 months before the eruption, which mostly
 852 shows a negative anomaly (i.e., anomaly < 1; Table 5; **Figure 9**, e). This precipitation anomaly
 853 shows a clear break at a value of 0.87, for which SHAP values are dominantly negative below
 854 and positive above. Above a value of 1, SHAP values increase. **Figure 9**, e shows a negative
 855 peak in SHAP values between an anomaly of 0.85–0.87 across all landcover classes but stronger
 856 for crops. Plotting SHAP values on a map (**Figure 9**, f), the spatial clustering of negative SHAP
 857 values corresponds to the location of crops between San Carlos de Bariloche and Comallo
 858 (**Figure 1**). No variable unequivocally explains this spatial clustering.

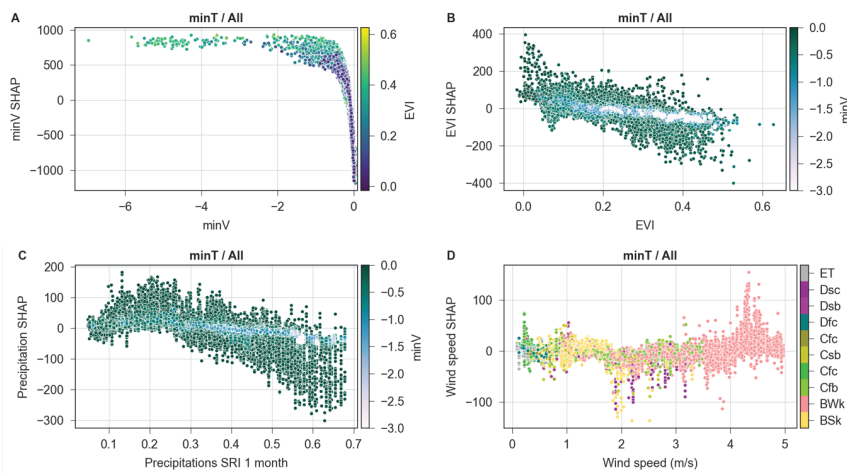
Deleted: Figure 9

Deleted: Figure 9

Deleted: Figure 9

Formatted: Font: Bold, English (UK)

Deleted: Figure 1



859

860 Figure 10: SHAP dependence plots for *minT* showing the effect on the SHAP value from **a** *minV* as a function of
 861 EVI; **b** EVI as a function of *minV*; **c** 1-month precipitation anomaly as a function of *minV* and **d** wind speed as a
 862 function of climate. Negative SHAP values contribute to decreasing *minT* and therefore decrease impact the
 863 duration for reaching *minV*.

864 Features driving *minT*

865 With a mean absolute SHAP value >7 times larger than any other variable, *minV* is by far the
 866 most important for predicting *minT* (Figure 10 a), with a cut-off between positive (i.e.,
 867 increasing the value of *minT*) and negative (i.e., decreasing *minT*) at a *minV* value of ~0.15. The

872 effect of EVI on $minT$ is the opposite of $minV$ (Figure 9, a): although high EVI values tend to
873 increase the impact magnitude (lower $minV$), they generally contribute to reducing the impact
874 duration (i.e., Figure 10 b). Interestingly, this trend disappears as $minV$ increases. This can be
875 explained by the fact that points affected by high $minV$ values in Figure 10 b are associated with
876 relatively high $minT$ values (Figure 7; Figure 10 a). These points are associated with damage
877 classes suggesting land retirement, and their recovery is therefore independent of the pre-
878 eruption EVI level. The 1-month precipitation anomaly is the 5th most important variable for
879 $minT$ (Figure 10 c), and SHAP values are mostly positive below an anomaly of 0.3 and mostly
880 negative above 0.5. As for EVI, high $minV$ values are less sensitive to the general trend. Finally,
881 Figure 10 d shows the effect of the wind speed at the time of eruption on $minT$ as a function of
882 the climate. Wind speeds >4 m/s considerably increase $minT$, especially in an arid climate (i.e.,
883 BWk) where the vegetation is mostly shrubs, herbaceous and sparse. Points with positive SHAP
884 values at wind speeds >4 m/s are characterized by accumulations of fine ash >0.5 kg/m². In
885 contrast, points with minimum SHAP values between wind speeds of 1.8–2.8 m/s correspond
886 to crops close to Piedra del Aguila and show fine ash loads <0.5 kg/m².

Deleted: Figure 9

Deleted: Figure 7

887 5. Discussion and perspectives

888 The proposed methodology provides a new framework to systematically assess the vulnerability
889 of vegetation to tephra fallout as a dynamic, multi-variate problem. Its application to the CC
890 2011 eruption highlights how big EO datasets and interpretable machine learning could help
891 acquiring a new knowledge from tens to hundreds of understudied eruptions recorded in
892 archives of multispectral images. This approach aligns with FAO's objective of gaining a global
893 understanding of vegetation vulnerability through the systematic study of their impacts and, in
894 turn, contributes to various Sustainable Development Goals (SDGs 2.4, 13.1, 15.3). Specific to
895 volcanic risk, this is the first effort to provide a large scale, quantitative basis to estimate the

898 impacts of explosive volcanic eruptions on food production. On a longer time-scale and large
899 spatial scale, this is the first step towards tackling the unaddressed *black elephant* event that is
900 the risk of future large eruptions on food security (Lin et al., 2021).

901 **Validation and causal inference**

902 Our methodology ~~attempts to highlight~~ impact mechanisms either occurring from the direct
903 action or arising from interactions between physical properties. Since we neglect the impact
904 from water leachable elements (e.g., Stewart et al., 2020), the approach is more suited to
905 dominantly magmatic events rather than eruptions with a significant hydrothermal component.
906 Impact patterns captured by our methodology are corroborated by lessons learned from
907 empirical post-EIA and experiments. For CC 2011, the model suggests that, except for points
908 subjected to destruction from large tephra loads, various biotic and abiotic variables tend to
909 have a more critical control on both impact magnitude and impact duration than deposit

910 properties (**Table 5**). SHAP dependence plots for deposit properties (e.g., **Figure 8**, a–e) identify
911 similar tephra thresholds as those in existing DDS (**Table 1**). Nevertheless, ~~numerous evidences~~
912 ~~reported in post-EIA as well as controlled experiments outline the dependency of impact~~
913 ~~mechanisms~~ to size distribution, ranging from physical impact for large lapilli to a reduction of
914 light interception from fine ash leading to a decrease in photosynthesis (e.g., Ligot et al., 2022).

915 DDS must therefore consider other hazard impact metrics than only tephra thickness, and Fig.
916 8–10 are the first attempt towards this objective. The method is also able to capture impacts
917 arising from interaction between other parameters than deposit properties. For instance, **Figure**
918 **9** d suggests that the model captures the general relationship between presence of ash,
919 precipitation (inferred from climate) and wind speed in controlling the impact from aeolian
920 remobilisation. This demonstrates the ability of the model to identify complex and dynamic
921 processes, and cross-validating thresholds inferred from the model with values from existing
922 post-EIA and experiments provides a systematic framework to generalize observations made at

Deleted: of impact mechanisms

Deleted: focuses on

Deleted: Table 5

Deleted: Figure 8

Deleted: identified

Deleted: Table 1

Deleted: recent findings

Deleted: from

Deleted: (e.g., Ligot et al., submitted; Ligot et al., in prep).

Deleted: Figure 9

933 different scales (Dominguez et al., 2020a; Forte et al., 2017; Leadbetter et al., 2012; Liu et al.,
934 2014).

935 Despite these observations, methodologies for interpretable ML should be carefully used when
936 attempting to infer causality from correlations/associations. Suggestions of causality are
937 currently restricted to effects that rely on phenomena that have been either witnessed in the field
938 or experiments. Other variables considered in our dataset show conspicuous and complex
939 patterns that we are unable to explain (e.g., [Figure 8](#) f, [Figure 9](#) e). Such patterns have two
940 possible explanations (or a combination of both): either the model fails to accurately capture
941 the underlying relationship between feature and target variable, or the relationship is
942 complicated by other factors (e.g., feature interactions, confounding variables), including
943 unobserved ones. Investigating which association captures true causality therefore requires the
944 development of synergies between various relevant disciplines (e.g., physical volcanology,
945 ecology, soil sciences, disaster risk reduction). The development and adaptation of existing
946 causal inference methods in Earth Sciences to investigate a system's causal interdependencies
947 is an active topic of research (Runge et al., 2019).

948 **Towards a model for agricultural crops and food production**

949 The methodology currently relies on the CGLS-LC100 land cover dataset do distinguish
950 between natural vegetation and agriculture. We focus here on agricultural crops which, despite
951 representing ~1% of the study area, show the highest vulnerability to tephra fall ([Figure 9](#)).
952 Note that although pastoral crops are included in the *Herbaceous vegetation* class in CGLS-
953 LC100, it is impossible to distinguish between natural and managed grassland (Buchhorn et al.,
954 2020). Post-EIA on agricultural impacts have demonstrated how agriculture vulnerability
955 depends on various factors that are not included in our model, including some of socio-
956 economic nature (Blake et al., 2015; Ligot et al., 2022; Magill et al., 2013; Phillips et al., 2019;
957 Wilson et al., 2013a, 2007) that reflect specific challenges associated with different farming

Deleted: Figure 8

Deleted: Figure 9

Deleted: Figure 9

961 activities (e.g., pastoral versus horticultural, intensive versus subsistence farming). Although
962 future evolutions of the CGLS-LC100 dataset will possibly include finer sub-definitions of the
963 crops class (e.g., irrigated versus rainfed cropland, farm size; [Buchhorn et al., 2020](#)), the
964 methodology currently considers all agricultural crops as a uniform system.

965 Despite this limitation, the proposed methodology nevertheless follows impact mapping
966 techniques implemented in several other approaches for vegetation and food security mapping
967 and monitoring (e.g., Meroni et al., 2019; Poortinga et al., 2018; Rembold et al., 2019), but
968 differ in their fundamental purposes. To our knowledge, we provide here the first attempt to
969 combine numerical modelling, big EO data and ML into a framework to re-analyse and extract
970 new knowledge from data recorded in decades of remote sensing images as the basis for a new
971 type of evidence-based vulnerability model. However, several steps are required for future
972 evolutions of our approach to inform quantitative risk assessments on food production and
973 security. Amongst them, future iterations of the methodology will focus on achieving:

- 974 1. More applications of the model to various types of climates, eruptions and sampling
975 different relationship between eruption date and phenological cycle in order to improve
976 its generalisation;
- 977 2. Comparison, validation and scaling of the EVI-based impact metrics with other impact
978 estimates, either based on field interviews (e.g., yield loss), mapping (e.g., percentage
979 of destroyed or damage vegetation) or other indirect proxies for physical processes (e.g.,
980 Gross and Net Primary Productivity);
- 981 3. The inclusion of parameters describing the recovery of vegetation (i.e., the shape of the
982 CDI curve after reaching $minV/minT$; **Figure 3**).

983 **Caveats and future research**

984 Below are future challenges and possible improvements of the method.

Deleted: .

- 986 1. The methodology takes advantage of datasets available on GEE ([Table 2](#)) and combines
 987 datasets of different nature, spatial and temporal resolutions. This discrepancy affects
 988 the accuracy of the model, and future development will explore a balance between the
 989 spatial and temporal resolutions of all datasets. Specifically ERA5 data will be
 990 reanalysed using mesoscale atmospheric models (e.g., Skamarock et al., 2019) at a
 991 resolution consistent with other datasets;
- 992 2. An inherent and inevitable dependency exists between the various datasets; some are of
 993 ecological nature (e.g., [multicollinearity between elevation, climate, landcover,](#)
 994 precipitation and temperature) whereas other are geographic coincidences (e.g., lapilli
 995 dominantly affect the Cfb climate class, [Figure 1](#)). Further work is necessary to explore
 996 how these dependences influence model prediction and interpretability;
- 997 3. The methodology currently [attempts to capture impact as a function of](#) pre-eruption
 998 [variables \(e.g., rainfall anomaly for various time steps before the eruption\)](#). In order to
 999 capture post-eruptive [processes in impact modelling](#), future applications of the model
 1000 will include post-eruption variables in the training process (e.g., [wind speed and](#)
 1001 [precipitation after the eruption to capture ash residence on vegetation surface](#));
- 1002 4. Despite providing a satisfactory accuracy, other algorithms and models than gradient
 1003 boosted regression trees allowing multi-output predictions must be explored to model
 1004 *minV* and *minT* jointly;
- 1005 5. [The CDI was designed as a proxy for the long-term post-eruption evolution of the](#)
 1006 [biomass production expressed by the EVI. Unlike more frequently used anomaly indices](#)
 1007 [relying on a ratio between post- and pre-eruption conditions, the CDI aims at](#)
 1008 [quantifying a budget between losses and gains. Although this implies a correlation](#)
 1009 [between EVI and CDI \(section 3.1.2\), this approach allows defining indices similar to](#)
 1010 [minV and minT to capture recovery and investigate potential gains in biomass](#)

Deleted: Table 2

Deleted: is a function of

Deleted: Figure 1

Deleted: relies only on

Deleted: values for covariates

Deleted: the evolution of

Deleted: aspects

Deleted: (e.g., ash residence on vegetation surface as a function of wind and precipitations)

Deleted: ;

1021 production following eruptions. Future work, along with accounting for post-eruption
1022 variables and multi-output predictions, will consider aspects of recovery in the model:

- 1023 6. ML models used in EO applications rarely accommodate spatial (and spatio-temporal)
1024 dependence. Accounting for these is necessary for reliable (causal) inference and
1025 uncertainty quantification. We plan to investigate the use of Gaussian processes, among
1026 others, to capture any residual spatial dependence.

1027 6. Conclusion

1028 We developed a methodology to remotely quantify impact through a combination of big EO
1029 data, interpretable ML and physical volcanology as a first step towards the development of a
1030 framework to identify, quantify and generalize key variables driving the impact of vegetation
1031 after an eruption. The methodology is designed to provide a high-level and complementary
1032 perspective to dedicated studies of the various disciplines involved in the characterization of
1033 the vulnerability and impact of vegetation and crops to natural hazards beyond tephra fallout,
1034 and has the potential to enhance the development of new synergies between the different actors
1035 and stakeholders involved in this specific facet of risk management.

1036 Based on the application of the methodology to the 2011 eruption of Cordon Caulle, the main
1037 conclusions are:

- 1038 - Both the magnitude and the duration components of impact captured by the processing
1039 of MODIS satellite imagery reflect the geometry of the deposit (**Figure 5**);
- 1040 - The methodology provides a systematic approach to identify the nature of the most
1041 important variables controlling the final impact metrics. The forest landcover class is
1042 mostly controlled by deposit properties (e.g., lapilli accumulation), whereas the crops
1043 landcover class predominantly depends on biotic and abiotic parameters;

Deleted: Figure 5

- 1045 - Interpretable machine learning methods provide insights into the nature of impacts. For
1046 instance, forests appear to be impacted by a direct physical impact caused by heavy
1047 accumulations;
- 1048 - Across landcover classes present in the study area, SHAP dependence plots suggest that
1049 forest and crops are the most and the least resilient vegetation classes to tephra
1050 accumulation, respectively ([Figure 9, c](#));
- 1051 - The interpretation of SHAP dependence plots for deposit properties of the different
1052 landcover classes ([Figure 8](#)) are in good agreement with thresholds for existing DDS
1053 inferred from post-event impact assessments ([Table 1](#)), which further reinforces the
1054 validity and usefulness of our approach.

Deleted: Figure 9

Deleted: Figure 8

Deleted: Table 1

1055 **Author contribution**

1056 SB designed the project, elaborated the methodology and wrote the Python library with inputs
1057 from all co-authors on aspects of volcanic risk (SFJ, TW), interactions between tephra deposits
1058 and vegetation (PD) and data science (WHA). All authors contributed to the manuscript.

1059 **Competing interests**

1060 The authors declare that they have no conflict of interest.

1061 **Acknowledgements**

1062 We are grateful to Edwin Tan and EOS/ASE's HPC for support on the Gekko cluster, to Lucia
1063 Dominguez for providing isopach maps, to Jan Peuker for his patience and advice for the
1064 development of ML modelling strategies, and to Oege Dijk for developing the
1065 *explainerdashboard* library. [We also would like to thank Matthieu Kervyn and one anonymous](#)
1066 [reviewer for constructive comments as well as Giovanni Macedonio for his role as editor.](#) This
1067 work was supported by the National Research Foundation Singapore and the Ministry of
1068 Education—Singapore under the Research Centres of Excellence initiative (SB, SJ).

1072 **References**

1073 Automatic citation updates are disabled. To see the bibliography, click Refresh in the Zotero
1074 tab.